

# Suppressing the Jahn–Teller Effect in Mn-Based Layered Oxide Cathode toward Long-Life Potassium-Ion Batteries

Zhitong Xiao, Fanjie Xia, Linhan Xu, Xuanpeng Wang,\* Jiashen Meng, Hong Wang, Xiao Zhang, Lishan Geng, Jinsong Wu, and Liqiang Mai\*

Mn-based layered oxides are one of the most appealing cathodes for potassium-ion batteries (PIBs) because of their high theoretical capacity. However, the Jahn–Teller effect of  $Mn^{3+}$  induces detrimental structural disorder and irreversible phase transition, leading to inferior cycling stability. Herein, an efficient strategy to suppress the Jahn–Teller effect in Mn-based layered oxides by regulating the Mn average valence is demonstrated. To verify this strategy,  $Ti^{4+}$  and  $Mg^{2+}$  ions are chosen and introduced into the layered oxides ( $K_{0.5}Mn_{0.7}Co_{0.2}Fe_{0.1}O_2$ ), which can enhance the structural stability but have opposite effects on the regulation of  $Mn^{3+/4+}$  valence. The  $K_{0.5}Mn_{0.6}Co_{0.2}Fe_{0.1}Mg_{0.1}O_2$  with a higher Mn valence (4+) exhibits long-term cycling stability as a PIB cathode compared to the  $K_{0.5}Mn_{0.6}Co_{0.2}Fe_{0.1}Ti_{0.1}O_2$  with a lower Mn valence (3.667+). Meanwhile, the detrimental phase transition from P3 to O3 caused by Jahn–Teller effect is completely suppressed, and is replaced by a highly reversible single-phase solid solution reaction for  $K_{0.5}Mn_{0.6}Co_{0.2}Fe_{0.1}Mg_{0.1}O_2$ . The enhanced cycling stability and single-phase reaction are attributed to the suppressed Jahn–Teller effect via Mn valence regulation, confirmed by first-principles calculations. Therefore, this discovery paves the way for the development of advanced layered cathodes for the next-generation high-performance PIBs.

shortage of high-performance cathode materials is one of the essential barriers for developing next generation high-power and high-energy-density PIBs.<sup>[5–8]</sup> Compared to other cathode materials,  $K^+$ -contained layered transition metal oxides ( $K_xTMO_2$ ; TM = Mn, Co, Fe, Ni, Mg, Ti, etc.) are of great fascination due to the high theoretical capacities, suitable voltage platforms, and expedient synthesis process.<sup>[9–12]</sup> In particular, benefiting from cost reduction, environmental friendliness, and comparatively stable framework, Mn-based layered oxides have been widely explored in PIBs.<sup>[13–15]</sup> However, these materials usually suffer from inferior cycling performance, which have limited their future applications.<sup>[16–18]</sup>

The poor cycling performance is essentially originated from Jahn–Teller distortion in the Mn-based layered oxides. Mn element usually exists in the mixed valence state of  $Mn^{3+}$  and  $Mn^{4+}$ .<sup>[19–21]</sup> Among them,  $Mn^{4+}$  can form the undistorted (ideal)  $[MnO_6]$  octahedra, forming a stable crystal structure. However, the

high-spin  $Mn^{3+}$  with the electron configuration of  $(t_{2g})^3(e_g)^1$  in the 3d orbital usually produces a Jahn–Teller distortion. This geometric distortion with two longer and the other two shorter Mn–O axial bonds (other than the equatorial Mn–O bonds in structure without distortion), usually reduces the symmetry and energy of nonlinear molecular system, and leads to a

## 1. Introduction

As a promising substitute to lithium-ion batteries for large-scale energy storage, potassium-ion batteries (PIBs) have aroused intense concern because of plentiful potassium resource and low  $K^+/K$  redox potential ( $-2.936$  vs  $E^0$ ).<sup>[1–4]</sup> Nonetheless, the

Z. Xiao, F. Xia, J. Meng, H. Wang, X. Zhang, L. Geng, J. Wu, L. Mai  
State Key Laboratory of Advanced Technology for Materials Synthesis and Processing  
Wuhan University of Technology  
Wuhan 430070, P. R. China  
E-mail: mlq518@whut.edu.cn  
F. Xia, H. Wang, J. Wu  
Nanostructure Research Center (NRC)  
Wuhan University of Technology  
Wuhan 430070, P. R. China

L. Xu  
Department of Physics  
Collaborative Innovation Centpotassiumer for Optoelectronic Semiconductors and Efficient Devices  
Xiamen University  
Xiamen 361005, P. R. China

X. Wang  
Department of Physical Science & Technology  
School of Science  
Wuhan University of Technology  
Wuhan 430070, P. R. China  
E-mail: wxp122525691@whut.edu.cn

X. Wang, L. Mai  
Foshan Xianhu Laboratory of the Advanced Energy Science and Technology Guangdong Laboratory  
Xianhu Hydrogen Valley  
Foshan 528200, P. R. China

 The ORCID identification number(s) for the author(s) of this article can be found under <https://doi.org/10.1002/adfm.202108244>.

DOI: 10.1002/adfm.202108244

structural disorder and a strong strain in the structure.<sup>[22–24]</sup> In addition, during the charging and discharging processes, Mn valence will fluctuate between +3 and +4, introducing repeated removal and restoration of Jahn–Teller distortion, which causes the irreversible multiphase transition.<sup>[24–27]</sup> Therefore, the structural instability ascribed to serious Jahn–Teller distortion of massive trivalent manganese is the main source for the rapid capacity fading in the Mn-based layered oxides.<sup>[28,29]</sup> Based on this, increasing the average valence of Mn from +3 to +4 may have important meaning to improve the cycling stability of Mn-based layered oxides.

The problems caused by the Jahn–Teller effect are also existed in similar Na<sup>+</sup>-contained Mn-based layered oxide systems.<sup>[30]</sup> Partial substitution of Mn by electrochemically active and/or inactive transition metal elements, such as Li, Co, Ni, Zn, and Ti, is an efficient approach.<sup>[31–33]</sup> For instance, Zhang et al.<sup>[33]</sup> prepared a Zn-doped Na<sub>0.833</sub>Li<sub>0.25</sub>Mn<sub>0.7125</sub>Zn<sub>0.0375</sub>O<sub>2</sub> electrode material with an enhanced sodium storage performance. The doped Zn decreases the amount of Mn<sup>3+</sup> and mitigates the structural variations of [MnO<sub>6</sub>] octahedra, which not only suppresses the Jahn–Teller distortion but also improves phase stability. The ion doping strategy is also reported in K<sup>+</sup>-contained Mn-based layered oxide materials.<sup>[34–36]</sup> For example, Zhang et al.<sup>[37]</sup> designed a 5% Co-doped Mn-based layered oxide (K<sub>0.3</sub>Mn<sub>0.95</sub>Co<sub>0.05</sub>O<sub>2</sub>) with good cycling capability with capacity retention of 75% after 500 cycles. The Jahn–Teller effect is successfully prohibited by doping Co, leading to more isotropic K<sup>+</sup> migration pathways, thus improving the ionic diffusion and cycling stability. Similarly, Bai et al.<sup>[38]</sup> developed a Ni-doped K<sub>0.67</sub>Ni<sub>0.17</sub>Mn<sub>0.83</sub>O<sub>2</sub> material with enhanced cycling property (75% capacity retention cycled at 500 mA g<sup>-1</sup> after 200 cycles). Although the Jahn–Teller effects have been explored by some of the works, there is still no systematic studies carried out so far, on the intrinsic relation of Jahn–Teller effect and Mn valence on the electrochemical properties.

Herein, to explore the effect of the Mn average valence regulating on Jahn–Teller effect and the function on the electrochemical property in PIBs, we first synthesized a series of K-contained layered oxides with different Mn contents (K<sub>0.5</sub>Mn<sub>0.9-x</sub>Co<sub>x</sub>Fe<sub>0.1</sub>O<sub>2</sub>, *x* = 0.1, 0.2, 0.3, and 0.4). Due to charge compensation, the Mn average valence increases from 3.625+ to 4+ with the reduced Mn content. As the Mn average valence increased, two pairs of redox peaks in the high-voltage region were gradually weakened and then disappeared, and the cycling stability of the layered oxides material was improved. These results were mainly attributed to the efficient suppression of Jahn–Teller effect in local structures because of the increase of Mn average valence. Furthermore, in this work, the Mn<sup>3+/4+</sup> valence was also regulated via partial substitution of Mn by Mg<sup>2+</sup> and Ti<sup>4+</sup>. Both electrochemically inactive Mg<sup>2+</sup> and Ti<sup>4+</sup> usually function as structural stabilizers for layered oxides, thereby improving the cycling life.<sup>[39–41]</sup> Nevertheless, the regulating effects of divalent Mg and tetravalent Ti on the valence state of Mn<sup>3+/4+</sup> are opposite.<sup>[42]</sup> The obtained K<sub>0.5</sub>Mn<sub>0.6</sub>Co<sub>0.2</sub>Fe<sub>0.1</sub>Mg<sub>0.1</sub>O<sub>2</sub> with a high Mn valence exhibits superior cycling stability than that in K<sub>0.5</sub>Mn<sub>0.7</sub>Co<sub>0.2</sub>Fe<sub>0.1</sub>O<sub>2</sub> and K<sub>0.5</sub>Mn<sub>0.6</sub>Co<sub>0.2</sub>Fe<sub>0.1</sub>Ti<sub>0.1</sub>O<sub>2</sub> with the low Mn valence. A detailed analysis to explore the relation among the structure, electrochemical performance and structure evolutions were conducted

via a series of experimental measurements and first-principles calculations.

## 2. Results and Discussion

To reveal the correlation of Mn valence and Jahn–Teller effect, a series of K<sub>0.5</sub>Mn<sub>0.9-x</sub>Co<sub>x</sub>Fe<sub>0.1</sub>O<sub>2</sub> (*x* = 0.1, 0.2, 0.3, and 0.4) oxides are constructed and compared. From the inductively coupled plasma (ICP) measured results (Table S1, Supporting Information), the K:Mn:Co:Fe ratios of four materials are similar to the designed components. In the X-ray diffraction (XRD) patterns, all the diffraction peaks are assigned to the layered structure of four products (Figure 1a). X-ray photoelectron spectroscopy (XPS) test is performed to study the average valence state of materials. The spectra for Mn 2p<sub>3/2</sub> consist of Mn<sup>3+</sup> (642.0 eV) and Mn<sup>4+</sup> (642.64 eV), and the spectra for Mn 2p<sub>1/2</sub> are also composed of Mn<sup>3+</sup> (653.3 eV) and Mn<sup>4+</sup> (654.3 eV), which reveals the coexistence of Mn<sup>3+</sup> and Mn<sup>4+</sup> (Figure 1b).<sup>[22,37,43]</sup> Notably, the amount of Mn<sup>4+</sup> observably increases when the Mn content decreases gradually. For K<sub>0.5</sub>Mn<sub>0.5</sub>Co<sub>0.4</sub>Fe<sub>0.1</sub>O<sub>2</sub> sample, only the peaks of Mn<sup>4+</sup> can be observed. In the Co 2p spectra, the peaks at 780.28 and 795.21 eV are assigned to Co 2p<sub>3/2</sub> and Co 2p<sub>1/2</sub>, respectively, demonstrating that the Co oxidation state of four materials is +3 (Figure S1b, Supporting Information).<sup>[44]</sup> The peaks located at 710.9 and 724.2 eV are vested in Fe 2p<sub>3/2</sub> and Fe 2p<sub>1/2</sub>, respectively in the Fe 2p spectra, which identify the trivalent Fe state of those four materials (Figure S1c, Supporting Information).<sup>[22]</sup> According to the measured results, combined with the calculation of the charge compensation mechanism, the Mn average valence in K<sub>0.5</sub>Mn<sub>0.8</sub>Co<sub>0.1</sub>Fe<sub>0.1</sub>O<sub>2</sub>, K<sub>0.5</sub>Mn<sub>0.7</sub>Co<sub>0.2</sub>Fe<sub>0.1</sub>O<sub>2</sub>, K<sub>0.5</sub>Mn<sub>0.6</sub>Co<sub>0.3</sub>Fe<sub>0.1</sub>O<sub>2</sub>, and K<sub>0.5</sub>Mn<sub>0.5</sub>Co<sub>0.4</sub>Fe<sub>0.1</sub>O<sub>2</sub> are 3.625+, 3.714+, 3.833+, and 4+, respectively (Figure 1c). These results indicated that the Mn average valence is promoted with the decreasing of trivalent Mn content.

The effect of the Mn average valence (thus the Jahn–Teller effect) to electrochemical performance was systematically studied. The cyclic voltammetry (CV) curves of the K<sub>0.5</sub>Mn<sub>0.9-x</sub>Co<sub>x</sub>Fe<sub>0.1</sub>O<sub>2</sub> in PIBs were measured from 1.5 to 3.9 V (vs K<sup>+/K</sup>). The K<sub>0.5</sub>Mn<sub>0.8</sub>Co<sub>0.1</sub>Fe<sub>0.1</sub>O<sub>2</sub> exhibits four pairs of redox couples at 2.26/1.96, 2.67/2.35, 3.25/2.82, and 3.87/3.56 V (Figure 1d). In general, two pairs of redox peaks at 2.26/1.96 and 2.67/2.35 V originate from the Mn<sup>3+/Mn<sup>4+</sup></sup> redox couple; while the other two pairs of redox couples at 3.25/2.82 and 3.87/3.56 V are ascribed to the redox reactions of Co<sup>3+/Co<sup>4+</sup></sup> and Fe<sup>3+/Fe<sup>4+</sup></sup>.<sup>[22,23]</sup> However, numerous Mn-based layered oxides without other electrochemically active elements also display redox peaks above 3.0 V.<sup>[13–18,40,41]</sup> Therefore, the Mn<sup>3+/Mn<sup>4+</sup></sup> redox reaction also contributed to the redox couples in the high voltage region. The voltage plateaus in the charge/discharge curves are in accordance with the CV curves redox peaks (Figure S2a, Supporting Information). When the Mn average valence increases from 3.625+ to 4+, the redox couples at high voltage range of 3.25/2.82 and 3.87/3.56 V gradually weakened and disappeared (Figure 1d–g). The same variation tendency of the corresponding voltage plateaus can be observed in their charge/discharge curves (Figure S2a–d, Supporting Information). The K<sub>0.5</sub>Mn<sub>0.6</sub>Co<sub>0.3</sub>Fe<sub>0.1</sub>O<sub>2</sub> and K<sub>0.5</sub>Mn<sub>0.5</sub>Co<sub>0.4</sub>Fe<sub>0.1</sub>O<sub>2</sub> show only two redox peaks at the low voltage range. Similarly,

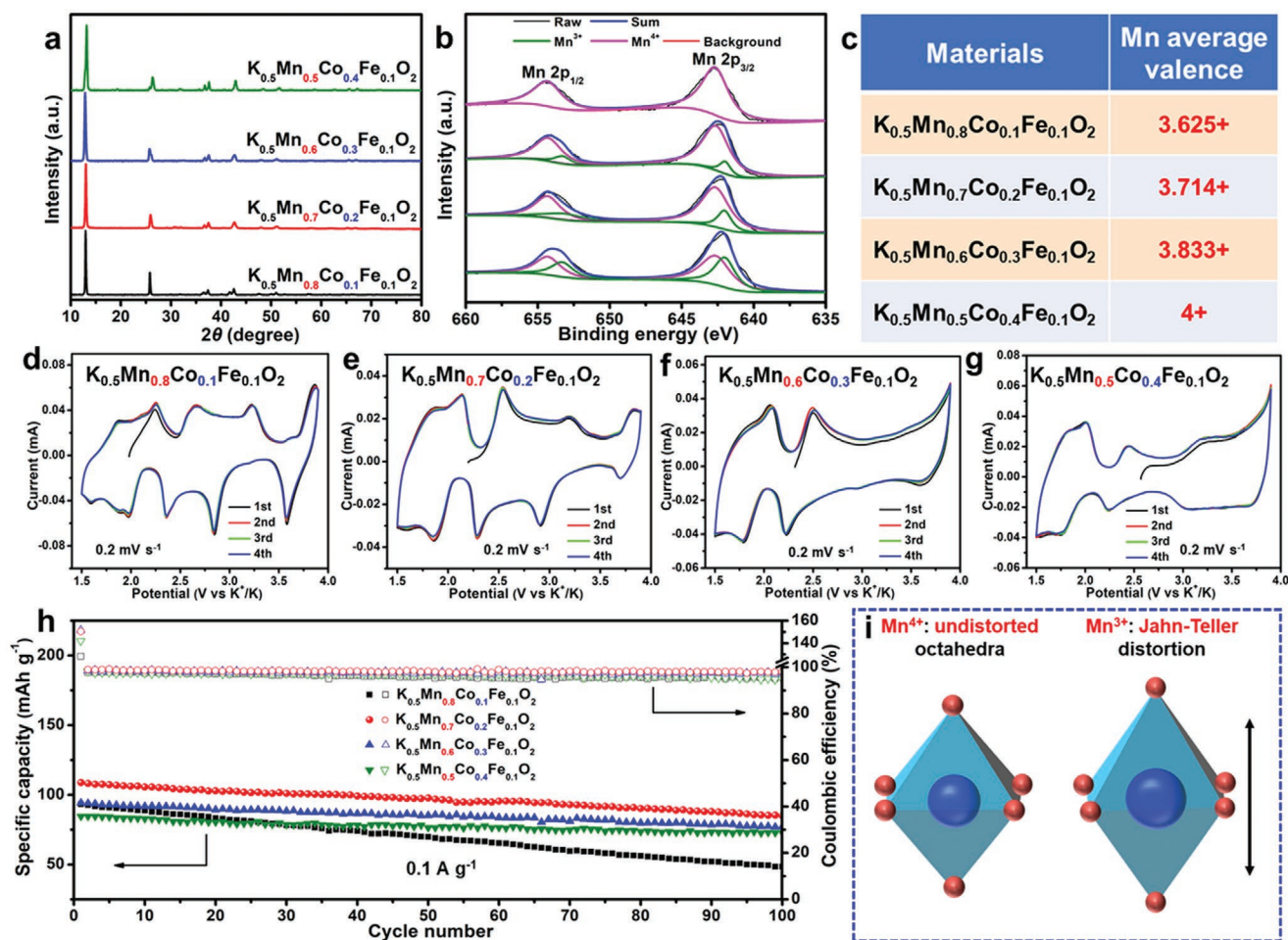


**Figure 1.** Illustration of Mn valence regulated Jahn–Teller effect and characterizations of  $K_{0.5}Mn_{0.9-x}Co_xFe_{0.1}O_2$ . a) XRD patterns. b) XPS spectra of Mn 2p. c) Comparison of Mn average valence. d–g) CV curves at  $0.2\text{ mV s}^{-1}$  of  $K_{0.5}Mn_{0.8}Co_{0.1}Fe_{0.1}O_2$ ,  $K_{0.5}Mn_{0.7}Co_{0.2}Fe_{0.1}O_2$ ,  $K_{0.5}Mn_{0.6}Co_{0.3}Fe_{0.1}O_2$ , and  $K_{0.5}Mn_{0.5}Co_{0.4}Fe_{0.1}O_2$ , respectively. h) Cycling property tested at  $0.1\text{ A g}^{-1}$ . i) Visualization of Jahn–Teller distortion.

the typical charge/discharge curves of two materials become sloping within high voltage range. The smooth charge/discharge curves in the high voltage region may be ascribed to the suppressed Jahn–Teller effect.<sup>[24]</sup> Notably, the Co and Fe still participated in the electrochemical reactions within high voltage range to provide charge compensation, but the redox reaction of Mn is inhibited. Moreover, the reasons and detailed explanation of possible mismatch between the average valence state and electrochemical test results are provided in Figures S3–S5 and Table S2 in the Supporting Information. Therefore, these results indicated that the redox reaction of Mn in the high voltage region is gradually suppressed when the Mn average valence increases from 3.625+ to 4+.

When measured at  $0.1\text{ A g}^{-1}$ , the  $K_{0.5}Mn_{0.5}Co_{0.4}Fe_{0.1}O_2$  with the highest Mn valence exhibits the best cycling capacity with a 86% capacity retention after 100 cycles (Figure 1h). With the decrease of Mn average valence state, the cycle stability of  $K_{0.5}Mn_{0.6}Co_{0.3}Fe_{0.1}O_2$ ,  $K_{0.5}Mn_{0.7}Co_{0.2}Fe_{0.1}O_2$ , and  $K_{0.5}Mn_{0.8}Co_{0.1}Fe_{0.1}O_2$  decreased successively (capacity retention of 82%, 78%, and 52%, respectively) (Figure 1h). In general, the undistorted (ideal)  $[MnO_6]$  octahedra is formed for  $Mn^{4+}$  and produces stable crystal structure (Figure 1i). However, the Jahn–Teller

effect caused by  $Mn^{3+}$  makes  $[MnO_6]$  octahedra induce geometric distortion, which usually accompanies with two longer or shorter Mn–O axial bonds unlike those of the equatorial Mn–O bonds (Figure 1i). The distorted octahedra reduces the symmetry and energy of nonlinear molecular system, leading to a structural disorder and a strong strain in the crystal structure. Therefore, the higher Mn average valence, the lower content of  $Mn^{3+}$  that leads to the destructive Jahn–Teller effect, thereby reducing the structural distortion of the layered oxide and improving the cycle stability. This series of measured results indicated that the Jahn–Teller effect was successfully suppressed through Mn valence regulation, leading to the enhanced cycling performance of Mn-based layered oxides.

In order to further explore the influence of Mn valence regulation on the Jahn–Teller effect,  $K_{0.5}Mn_{0.6}Co_{0.2}Fe_{0.1}Ti_{0.1}O_2$  and  $K_{0.5}Mn_{0.6}Co_{0.2}Fe_{0.1}Mg_{0.1}O_2$  were synthesized. Both electrochemically inactive  $Ti^{4+}$  and  $Mg^{2+}$  ions usually function as structural stabilizers for layered oxides to enhance the cycling performance. However, tetravalent Ti and divalent Mg have opposite effects on the regulation of the valence state of  $Mn^{3+/4+}$ . The stoichiometric atomic ratios of the elements for three samples are confirmed by ICP measurement (Table S3, Supporting

Information). The actual molar ratios of all elements are close to the designated composition. In the Rietveld refined XRD patterns, all diffraction peaks of  $K_{0.5}Mn_{0.7}Co_{0.2}Fe_{0.1}O_2$ ,  $K_{0.5}Mn_{0.6}Co_{0.2}Fe_{0.1}Ti_{0.1}O_2$ , and  $K_{0.5}Mn_{0.6}Co_{0.2}Fe_{0.1}Mg_{0.1}O_2$  are assigned to the P3-type layered hexagonal structure (Figure 2a–c).<sup>[45]</sup> The corresponding P3-type crystal structures are depicted in the inset of Figure 2a–c and Figure S6 in the Supporting Information. The  $K^+$  are located at trigonal prismatic sites between the  $TMO_6$  octahedra (TM = Mn, Co, Fe, and Mg), and the O layers are stacked in the packing sequence of ABCCA.<sup>[24]</sup> The detailed structural information and refinement data of  $K_{0.5}Mn_{0.7}Co_{0.2}Fe_{0.1}O_2$ ,  $K_{0.5}Mn_{0.6}Co_{0.2}Fe_{0.1}Ti_{0.1}O_2$ , and  $K_{0.5}Mn_{0.6}Co_{0.2}Fe_{0.1}Mg_{0.1}O_2$  are presented in Tables S4–S6 in the Supporting Information. To gain more detailed crystal structure information in atomic-scale, aberration-corrected scanning transmission electron microscopy (STEM) with both a high-angle annular dark-field (HAADF) detector and an annular bright-field (ABF) detector was employed. The TM atoms are dark dots contrast in ABF-STEM image (Figure 2d,f) and bright

dots contrast in HAADF-STEM image (Figure 2e,g). Meanwhile, the less-bright dots contrast in HAADF-STEM image and the grey dotted contrast in ABF-STEM image are K layers. A crystal structure model is depicted in ABF-STEM image along the [010] zone axis for convenient visualization (Figure 2d). The O layers exhibit an ABCCA packing arrangement, and the K layers and TM layers are arranged alternately, which is well in agreement with the typical P3 phase (Figure 2d). The adjacent layer spacing is measured with about 0.70 nm in HAADF-STEM image (Figure 2e), which is consistent well with the XRD refinement data. The ABF-STEM image along the [001] zone axis shows the TM atom is surrounded by six other TM atoms and arranges to form a hexagonal symmetry (Figure 2f). The measured distance of adjacent TM atoms is 0.29 nm in HAADF-STEM images, which matches with the lattice parameter  $a$  (2.8836 Å) (Figure 2g). From the transmission electron microscopy (TEM) images (Figure S7a–c, Supporting Information), both  $K_{0.5}Mn_{0.7}Co_{0.2}Fe_{0.1}O_2$ ,  $K_{0.5}Mn_{0.6}Co_{0.2}Fe_{0.1}Ti_{0.1}O_2$ , and  $K_{0.5}Mn_{0.6}Co_{0.2}Fe_{0.1}Mg_{0.1}O_2$  materials show the particulate

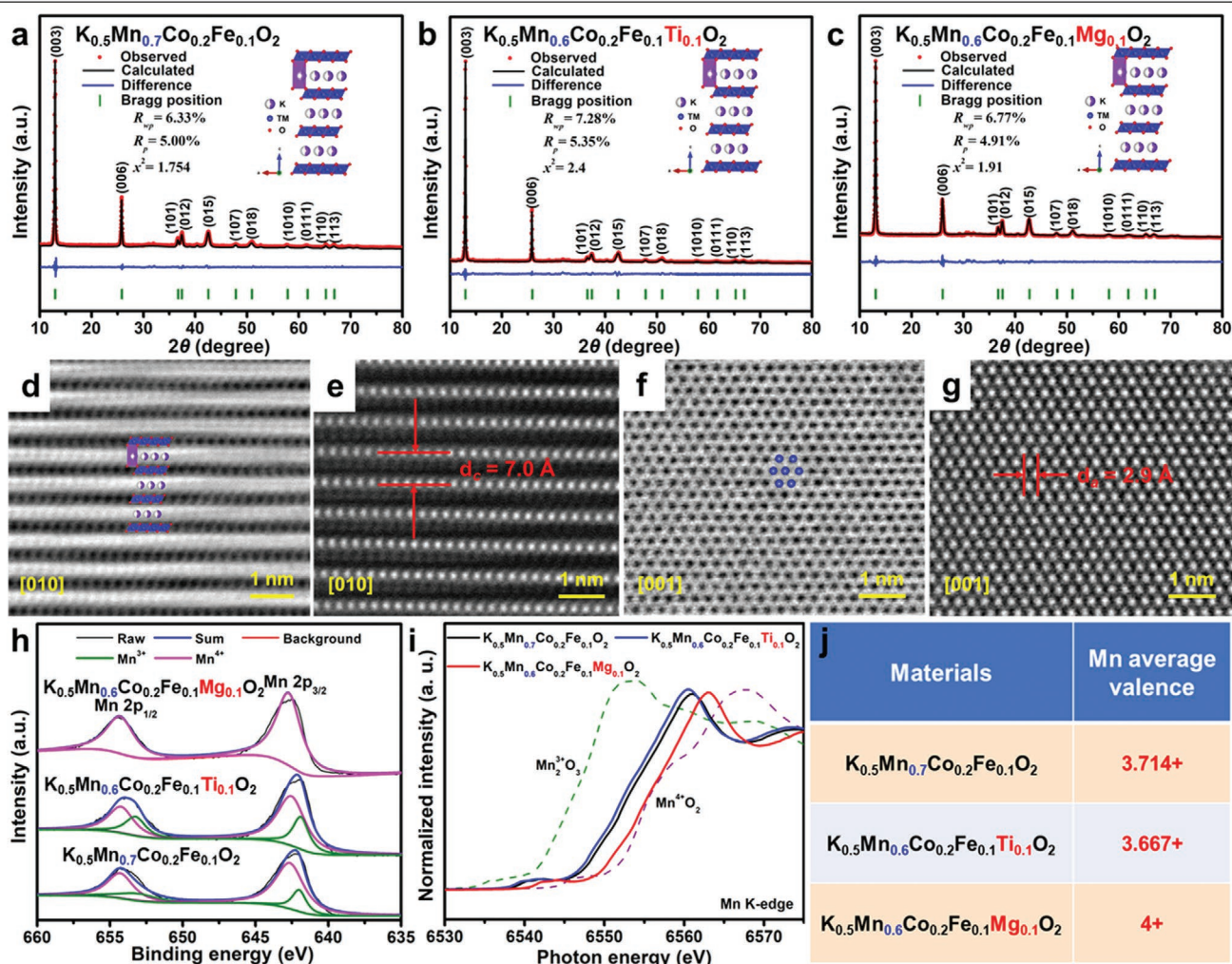


**Figure 2.** Characterizations of  $K_{0.5}Mn_{0.7}Co_{0.2}Fe_{0.1}O_2$ ,  $K_{0.5}Mn_{0.6}Co_{0.2}Fe_{0.1}Ti_{0.1}O_2$ , and  $K_{0.5}Mn_{0.6}Co_{0.2}Fe_{0.1}Mg_{0.1}O_2$ . XRD Rietveld refinement of a)  $K_{0.5}Mn_{0.7}Co_{0.2}Fe_{0.1}O_2$ , b)  $K_{0.5}Mn_{0.6}Co_{0.2}Fe_{0.1}Ti_{0.1}O_2$ , and c)  $K_{0.5}Mn_{0.6}Co_{0.2}Fe_{0.1}Mg_{0.1}O_2$ , respectively (inset: crystal structure viewed). d) ABF-STEM and e) HAADF-STEM images of  $K_{0.5}Mn_{0.6}Co_{0.2}Fe_{0.1}Mg_{0.1}O_2$  along the [010] zone axis. f) ABF-STEM and g) HAADF-STEM images of  $K_{0.5}Mn_{0.6}Co_{0.2}Fe_{0.1}Mg_{0.1}O_2$  along the [001] zone axis. h) XPS spectra of Mn 2p. i) XANES spectra of Mn K-edge. j) Comparison of Mn average valence.

morphology with 200–500 nm in diameter. The adjacent interplanar distances of three samples are all measured with 0.240 nm in high-resolution TEM (HRTEM) images, which is well agreement with the (012) peak (Figure S7d–f, Supporting Information). All of the inset selected area electron diffraction (SAED) patterns refer to the hexagonal structure (Figure S7d–f, Supporting Information). The energy dispersive X-ray spectroscopy (EDS) mapping images demonstrate the homogeneous distribution of all the elements, especially the introduced Ti and Mg elements (Figure S8, Supporting Information).

XPS spectra display that the valence states of Co and Fe in  $K_{0.5}Mn_{0.6}Co_{0.2}Fe_{0.1}Ti_{0.1}O_2$  and  $K_{0.5}Mn_{0.6}Co_{0.2}Fe_{0.1}Mg_{0.1}O_2$  are both 3+, indicating that the valence state of Co and Fe is retained after substitution (Figure S9b,c, Supporting Information). The Ti 2p spectrum of  $K_{0.5}Mn_{0.6}Co_{0.2}Fe_{0.1}Ti_{0.1}O_2$  shows a  $Ti^{4+}$  binding energies, which two peaks at 457.8 and 463.6 eV are assigned to Ti 2p<sub>3/2</sub> and Ti 2p<sub>1/2</sub>, respectively (Figure S9d, Supporting Information).<sup>[29]</sup> As for  $K_{0.5}Mn_{0.6}Co_{0.2}Fe_{0.1}Mg_{0.1}O_2$ , the Mg 1s spectrum displays a typical  $Mg^{2+}$  binding energies (1303.8 eV) (Figure S9e, Supporting Information).<sup>[40]</sup> In particular, after partial substituted of Mn by  $Ti^{4+}$ , the amount of  $Mn^{3+}$  in  $K_{0.5}Mn_{0.6}Co_{0.2}Fe_{0.1}Ti_{0.1}O_2$  is higher than that of  $K_{0.5}Mn_{0.7}Co_{0.2}Fe_{0.1}O_2$ , implying a decrease of the Mn valence state with Ti substituting (Figure 2h). In contrast to  $K_{0.5}Mn_{0.6}Co_{0.2}Fe_{0.1}Ti_{0.1}O_2$ , the observed binding energies of Mn 2p for  $K_{0.5}Mn_{0.6}Co_{0.2}Fe_{0.1}Mg_{0.1}O_2$  coincide well with  $Mn^{4+}$ , which implies an increase of the valence state of Mn with Mg substituting (Figure 2h). In order to further confirm the average oxidation states of Mn in  $K_{0.5}Mn_{0.7}Co_{0.2}Fe_{0.1}O_2$ ,  $K_{0.5}Mn_{0.6}Co_{0.2}Fe_{0.1}Ti_{0.1}O_2$ , and  $K_{0.5}Mn_{0.6}Co_{0.2}Fe_{0.1}Mg_{0.1}O_2$ , the X-ray absorption near edge structure (XANES) measurement was performed (Figure 2i). Compared with the reference spectra of  $Mn_2O_3$  and  $MnO_2$ , the average oxidation state of Mn in  $K_{0.5}Mn_{0.7}Co_{0.2}Fe_{0.1}O_2$  is an intermediate value between  $Mn^{3+}$  and  $Mn^{4+}$ . The photon energy of the Mn K-edge for  $K_{0.5}Mn_{0.6}Co_{0.2}Fe_{0.1}Ti_{0.1}O_2$  shifts to lower energy, which suggests a decrease of oxidation state of Mn after Ti substituted. Notably, XANES spectra of Mn K-edge show that the average oxidation state of Mn in  $K_{0.5}Mn_{0.6}Co_{0.2}Fe_{0.1}Mg_{0.1}O_2$  is close to 4+. These results indicate that the XANES measured conclusions are well consistent with the XPS analysis. According to the measured results combined with the calculation of the charge compensation mechanism, the Mn average valence in  $K_{0.5}Mn_{0.7}Co_{0.2}Fe_{0.1}O_2$ ,  $K_{0.5}Mn_{0.6}Co_{0.2}Fe_{0.1}Ti_{0.1}O_2$ , and  $K_{0.5}Mn_{0.6}Co_{0.2}Fe_{0.1}Mg_{0.1}O_2$  are 3.714+, 3.667+, and 4+, respectively (Figure 2j). This indicates that the Mn average valence is regulated by the introduction of Ti and Mg.

In order to identify the effect of Mn average valence state on Jahn–Teller effect, a series of electrochemical measurements were conducted while employing the substituted oxides as the PIB cathode (Figure 3). The CV curves of  $K_{0.5}Mn_{0.7}Co_{0.2}Fe_{0.1}O_2$  show distinct four pairs of redox couples at 2.13/1.85, 2.54/2.29, 3.19/2.90, and 3.83/3.70 V (Figure 3a). The CV curves of  $K_{0.5}Mn_{0.6}Co_{0.2}Fe_{0.1}Ti_{0.1}O_2$  with a lower Mn valence are similar to  $K_{0.5}Mn_{0.7}Co_{0.2}Fe_{0.1}O_2$  and also display four pairs of redox peaks (Figure 3b). Notably, the  $K_{0.5}Mn_{0.6}Co_{0.2}Fe_{0.1}Mg_{0.1}O_2$  with a higher Mn valence shows only two pair of redox couples at 2.13/1.85 and 2.54/2.29 V (Figure 3c). It is indicating that the two pairs of redox couples in the high voltage region disap-

pear when the Mn average valence increases from 3.714+ to 4+, whereas the decrease in the valence state of Mn have no effect on the electrochemical reaction. When measured at 0.1 A g<sup>-1</sup>,  $K_{0.5}Mn_{0.6}Co_{0.2}Fe_{0.1}Mg_{0.1}O_2$  with the highest Mn valence exhibits superior cycling capacity of 89.2 mAh g<sup>-1</sup> with a capacity retention of 91% after the 150 cycles (Figure 3g). Although Ti substitution can improve the cycle stability to a certain extent, the lower valence of Mn does not further prolong cycle life of  $K_{0.5}Mn_{0.6}Co_{0.2}Fe_{0.1}Ti_{0.1}O_2$  (80.2 mAh g<sup>-1</sup> with a capacity retention of 78%). In contrast, the unsubstituted  $K_{0.5}Mn_{0.7}Co_{0.2}Fe_{0.1}O_2$  with a low Mn valence shows inferior cycling performance of 70.3 mAh g<sup>-1</sup> with a capacity retention of 65%. The mechanism behind the cycle stability can be analyzed from the charge/discharge curves of different cycles (Figure 3d–f). After continuous charging/discharging process, the voltage platforms of  $K_{0.5}Mn_{0.7}Co_{0.2}Fe_{0.1}O_2$  above 2.8 V are gradually disappeared; while these voltage platforms of  $K_{0.5}Mn_{0.6}Co_{0.2}Fe_{0.1}Ti_{0.1}O_2$  have been retained to some extent (Figure 3d,e). In contrast, as no voltage platforms appear above 2.8 V, the charge and discharge curves are nearly overlapped, suggesting the good reversibility of  $K_{0.5}Mn_{0.6}Co_{0.2}Fe_{0.1}Mg_{0.1}O_2$  (Figure 3f). This implies that the main reason for the decrease in the capacity of those electrode material is the fading of the redox reactions in the high voltage region. Therefore, the enhanced cycling performance is attributed to the successfully suppressed Jahn–Teller effect through Mn valence regulated. In particular, the  $K_{0.5}Mn_{0.6}Co_{0.2}Fe_{0.1}Mg_{0.1}O_2$  electrode exhibits outstanding long-term cycling capability with high capacity retention of 78% after 150 cycles and 74% even after 500 cycles at 1 A g<sup>-1</sup> (Figure 3h). In addition, the  $K_{0.5}Mn_{0.6}Co_{0.2}Fe_{0.1}Mg_{0.1}O_2$  also exhibits good rate property with average discharge capacities of 104.6, 94.7, 88.2, 83.1, 77.2, 68.2, and 57.8 mAh g<sup>-1</sup> at 0.05, 0.1, 0.2, 0.3, 0.5, 1, and 2 A g<sup>-1</sup>, respectively (Figure S10a, Supporting Information). Meanwhile, the  $K_{0.5}Mn_{0.7}Co_{0.2}Fe_{0.1}O_2$  exhibits the corresponding discharge capacities of 114.3, 106.8, 97.8, 93.5, 86.4, 77.4, and 66.5 mAh g<sup>-1</sup>, respectively. The  $K_{0.5}Mn_{0.6}Co_{0.2}Fe_{0.1}Ti_{0.1}O_2$  electrode exhibits the corresponding capacities of 109.1, 99.5, 91.4, 84.3, 75.1, 64.4, and 54.0 mAh g<sup>-1</sup>, respectively. The charge/discharge curves of rate capability suggest low polarization of  $K_{0.5}Mn_{0.6}Co_{0.2}Fe_{0.1}Mg_{0.1}O_2$  (Figure S10b–d, Supporting Information). The galvanostatic intermittent titration technique (GITT) test is carried out to study the theoretical specific capacity of three electrode materials (Figure S11, Supporting Information). Before GITT test, the battery was charged to 3.9 V at 0.03 A g<sup>-1</sup>. The  $K_{0.5}Mn_{0.7}Co_{0.2}Fe_{0.1}O_2$ ,  $K_{0.5}Mn_{0.6}Co_{0.2}Fe_{0.1}Ti_{0.1}O_2$ , and  $K_{0.5}Mn_{0.6}Co_{0.2}Fe_{0.1}Mg_{0.1}O_2$  display theoretical discharge capacities of 129.9, 122.0, and 113.8 mAh g<sup>-1</sup> in GITT discharge test. Compared with layered oxide cathodes in previously reported, the  $K_{0.5}Mn_{0.6}Co_{0.2}Fe_{0.1}Mg_{0.1}O_2$  with a high Mn valence represents the remarkable electrochemical performances in PIBs (Table S7, Supporting Information).

The crystal structure evolutions of  $K_{0.5}Mn_{0.7}Co_{0.2}Fe_{0.1}O_2$ ,  $K_{0.5}Mn_{0.6}Co_{0.2}Fe_{0.1}Ti_{0.1}O_2$  and  $K_{0.5}Mn_{0.6}Co_{0.2}Fe_{0.1}Mg_{0.1}O_2$  during cycling are explored via in situ XRD measurement (Figure 4). When  $K^+$  extracted during the charge process, the (006) peak of  $K_{0.5}Mn_{0.6}Co_{0.2}Fe_{0.1}Mg_{0.1}O_2$  moves to a low angle, while the (101), (012), and (015) reflections move toward to a high angle (Figure 4g–i). These tendencies are ascribed to the contraction of

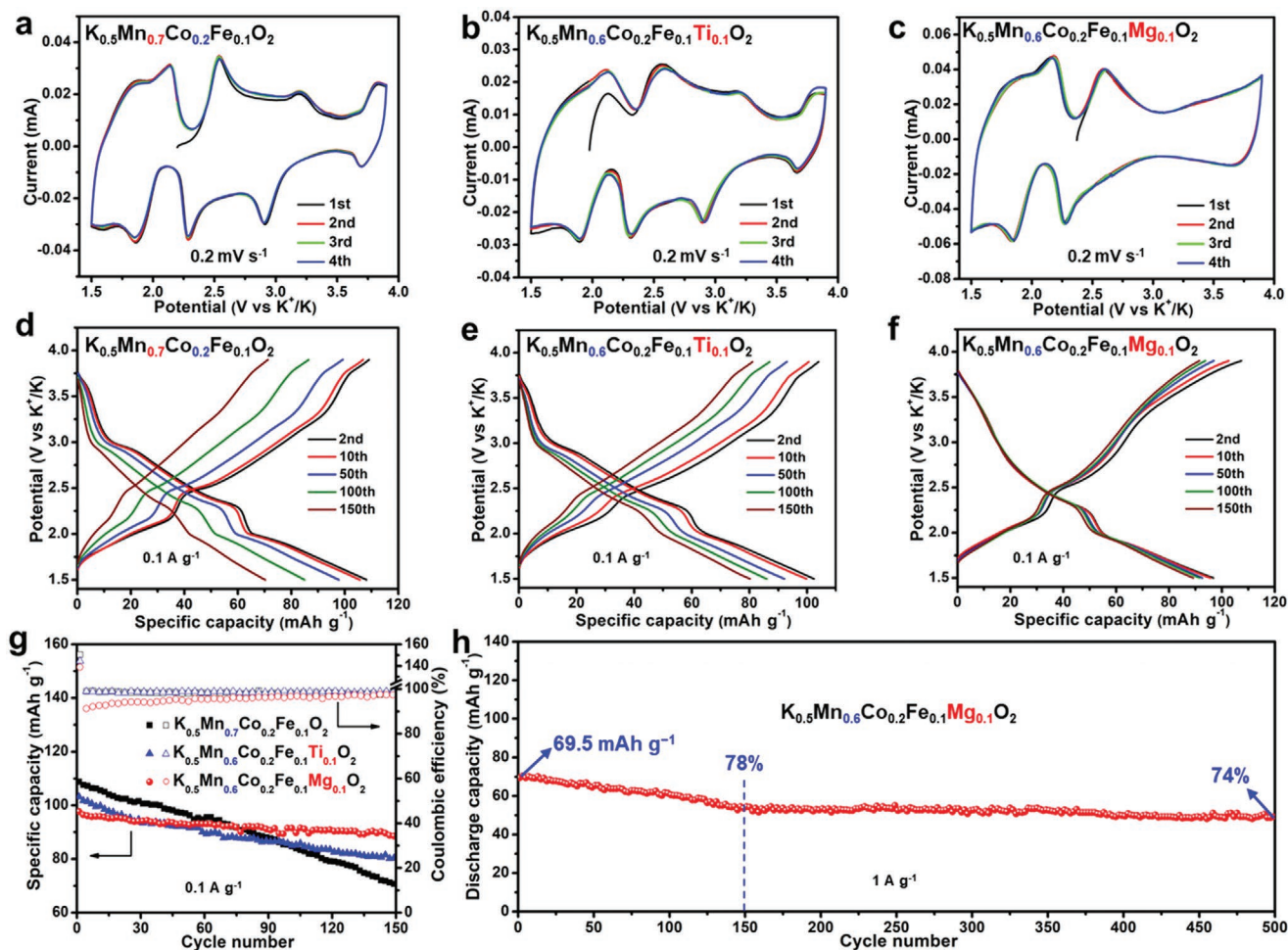


**Figure 3.** Electrochemical performances of  $\text{K}_{0.5}\text{Mn}_{0.7}\text{Co}_{0.2}\text{Fe}_{0.1}\text{O}_2$ ,  $\text{K}_{0.5}\text{Mn}_{0.6}\text{Co}_{0.2}\text{Fe}_{0.1}\text{Ti}_{0.1}\text{O}_2$ , and  $\text{K}_{0.5}\text{Mn}_{0.6}\text{Co}_{0.2}\text{Fe}_{0.1}\text{Mg}_{0.1}\text{O}_2$  in 1.5–3.9 V (vs  $\text{K}^+/\text{K}$ ). CV curves measured at  $0.2 \text{ mV s}^{-1}$  of a)  $\text{K}_{0.5}\text{Mn}_{0.7}\text{Co}_{0.2}\text{Fe}_{0.1}\text{O}_2$ , b)  $\text{K}_{0.5}\text{Mn}_{0.6}\text{Co}_{0.2}\text{Fe}_{0.1}\text{Ti}_{0.1}\text{O}_2$ , and c)  $\text{K}_{0.5}\text{Mn}_{0.6}\text{Co}_{0.2}\text{Fe}_{0.1}\text{Mg}_{0.1}\text{O}_2$ , respectively. Charge/discharge curves of d)  $\text{K}_{0.5}\text{Mn}_{0.7}\text{Co}_{0.2}\text{Fe}_{0.1}\text{O}_2$ , e)  $\text{K}_{0.5}\text{Mn}_{0.6}\text{Co}_{0.2}\text{Fe}_{0.1}\text{Ti}_{0.1}\text{O}_2$ , and f)  $\text{K}_{0.5}\text{Mn}_{0.6}\text{Co}_{0.2}\text{Fe}_{0.1}\text{Mg}_{0.1}\text{O}_2$ , respectively. g) Cycling property tested at  $0.1 \text{ A g}^{-1}$ . h) Long-term cycling performance of  $\text{K}_{0.5}\text{Mn}_{0.6}\text{Co}_{0.2}\text{Fe}_{0.1}\text{Mg}_{0.1}\text{O}_2$  at  $1 \text{ A g}^{-1}$ .

*a–b* plane and the enlargement of *c*-axis owing to the enhanced electrostatic repulsive interaction between O layers as  $\text{K}^+$  de-intercalated from interlayers.<sup>[12]</sup> Upon discharging, all peaks can reversibly reshift to in opposite directions. Notably, no new peaks of other phases are observed during the whole charge and discharge process. Therefore, the  $\text{K}_{0.5}\text{Mn}_{0.6}\text{Co}_{0.2}\text{Fe}_{0.1}\text{Mg}_{0.1}\text{O}_2$  experienced a typical reversible single-phase reaction with a consecutive peak shift during the  $\text{K}^+$  extraction/insertion process, demonstrating the phase and structure stability in electrochemical reaction. On the contrary, when charging from 3.4 V to discharging at 3.0 V, a new peak belonging to the (104) peak of O3 phase at around  $40.5^\circ$  is observed for  $\text{K}_{0.5}\text{Mn}_{0.7}\text{Co}_{0.2}\text{Fe}_{0.1}\text{O}_2$  and  $\text{K}_{0.5}\text{Mn}_{0.6}\text{Co}_{0.2}\text{Fe}_{0.1}\text{Ti}_{0.1}\text{O}_2$ ; while the (105) peak of P3 phase disappears in this range. This is suggesting that the  $\text{K}_{0.5}\text{Mn}_{0.7}\text{Co}_{0.2}\text{Fe}_{0.1}\text{O}_2$  and  $\text{K}_{0.5}\text{Mn}_{0.6}\text{Co}_{0.2}\text{Fe}_{0.1}\text{Ti}_{0.1}\text{O}_2$  undergo a phase transition between P3 and O3 phase at high potential (Figure 4a–f), which may cause structural degradation and rapid capacity fading.<sup>[12,45]</sup> Such a phase transition between P3 and O3 phase is mainly caused by the Jahn–Teller distortion of  $\text{Mn}^{3+}$  and the movement of  $\text{TMO}_6$  octahedra.<sup>[30,35]</sup> The Mg-substituted Mn-based layered oxide with a high Mn valence

mitigates the Jahn–Teller effect, which effectively suppresses the destructive phase transition. Nevertheless, Ti substitution can reduce the average valence of Mn and thus does not have this effect.

To further reveal the relationship of Mn valence state on Jahn–Teller effect, the partial density of states (PDOS) of Mn are calculated by first-principles calculations (Figure 5). In general, the Mn 3d electronic orbital includes two types:  $e_g$  ( $d_z^2$  and  $d_{x^2-y^2}$ ) and  $t_{2g}$  ( $d_{xz}$ ,  $d_{yz}$ ,  $d_{xy}$ ) for a  $\text{MnO}_6$  octahedra.<sup>[31]</sup> The  $t_{2g}$  orbitals of  $\text{Mn}^{4+}$  are fully occupied and the  $e_g$  orbitals are unoccupied.<sup>[46]</sup> All the  $\text{Mn}^{4+}$ –O bonds shared the same length as each other and the electronic cloud is also the same (Figure 5d). By comparison, the  $e_g$  orbitals of the  $\text{Mn}^{3+}$  will split into two orbitals of unoccupied  $d_{x^2-y^2}$  and occupied  $d_z^2$  near the Fermi level.<sup>[46]</sup> Due to the Jahn–Teller distortion, the elongated  $\text{Mn}^{3+}$ –O bond along the *z*-axis can weaken the electrostatic repulsion of the electron clouds between  $p_z$  orbital of  $\text{O}^{2-}$  in the octahedral corners and  $d_z^2$  orbital of  $\text{Mn}^{3+}$  in the octahedral center (Figure 5e).<sup>[46]</sup> For  $\text{K}_{0.5}\text{Mn}_{0.7}\text{Co}_{0.2}\text{Fe}_{0.1}\text{O}_2$  and  $\text{K}_{0.5}\text{Mn}_{0.6}\text{Co}_{0.2}\text{Fe}_{0.1}\text{Ti}_{0.1}\text{O}_2$ , the high energy  $e_g$  orbitals are split into two groups with one set under Fermi level and the other above Fermi level, which indicates

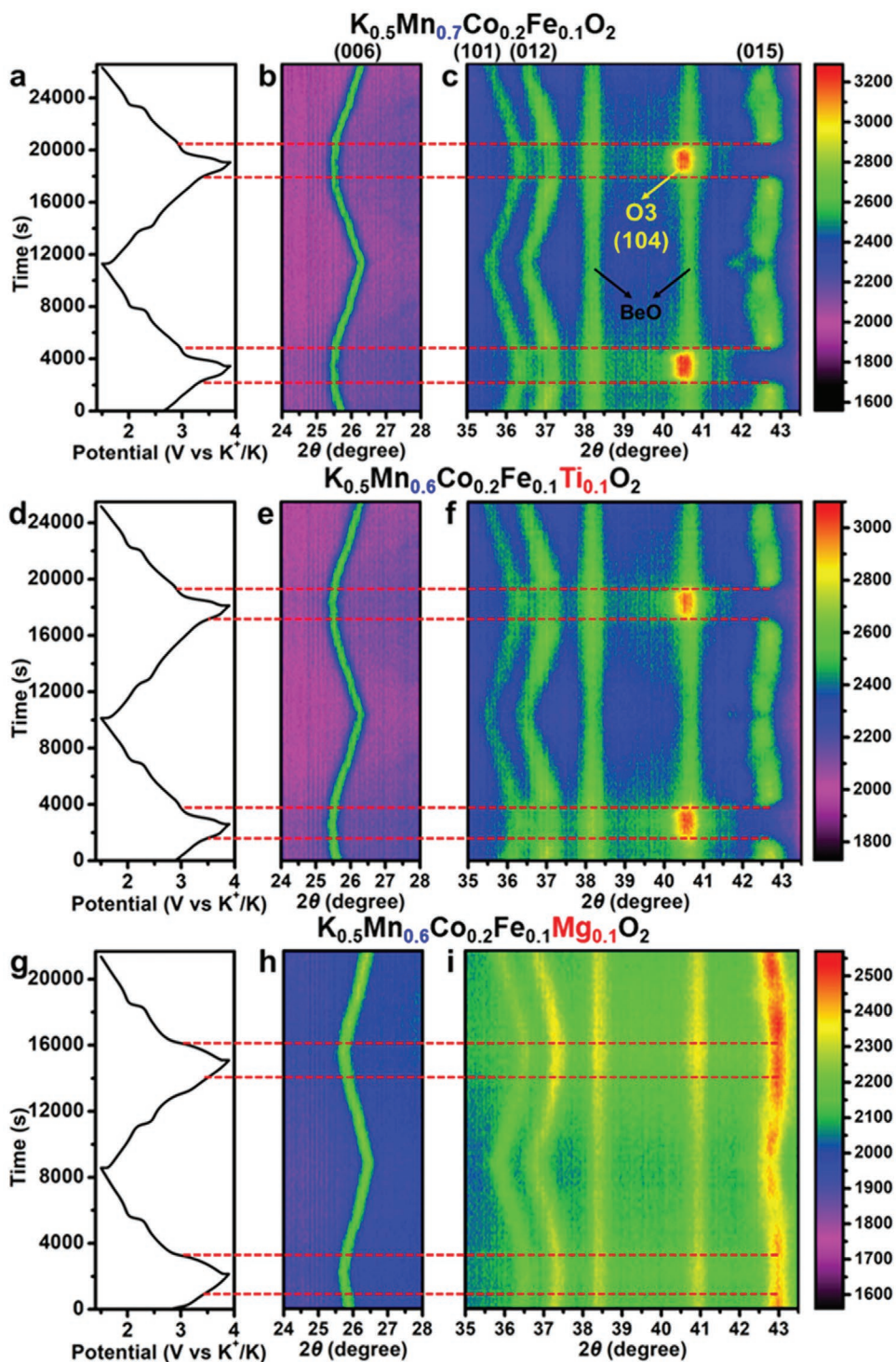


**Figure 4.** In situ XRD characterization of a–c)  $\text{K}_{0.5}\text{Mn}_{0.7}\text{Co}_{0.2}\text{Fe}_{0.1}\text{O}_2$ , d–f)  $\text{K}_{0.5}\text{Mn}_{0.6}\text{Co}_{0.2}\text{Fe}_{0.1}\text{Ti}_{0.1}\text{O}_2$ , and g–i)  $\text{K}_{0.5}\text{Mn}_{0.6}\text{Co}_{0.2}\text{Fe}_{0.1}\text{Mg}_{0.1}\text{O}_2$ .

the existence of Jahn–Teller active  $\text{Mn}^{3+}$  ions (Figure 5a,b).<sup>[31]</sup> In contrast, the  $e_g$  orbitals of Mn is not split, implying that the Mn in  $\text{K}_{0.5}\text{Mn}_{0.6}\text{Co}_{0.2}\text{Fe}_{0.1}\text{Mg}_{0.1}\text{O}_2$  is Jahn–Teller inactive  $\text{Mn}^{4+}$  ions (Figure 5c). This result proves theoretically that the undesired Jahn–Teller effect is efficiently suppressed by regulating the Mn valence.

### 3. Conclusion

As observed in the work, by accurately regulating the Mn valence, the Jahn–Teller effect can be effectively suppressed, thereby improving the cycling stability of Mn-based layered oxides. The Mn average valence was also regulated by partial substitution of

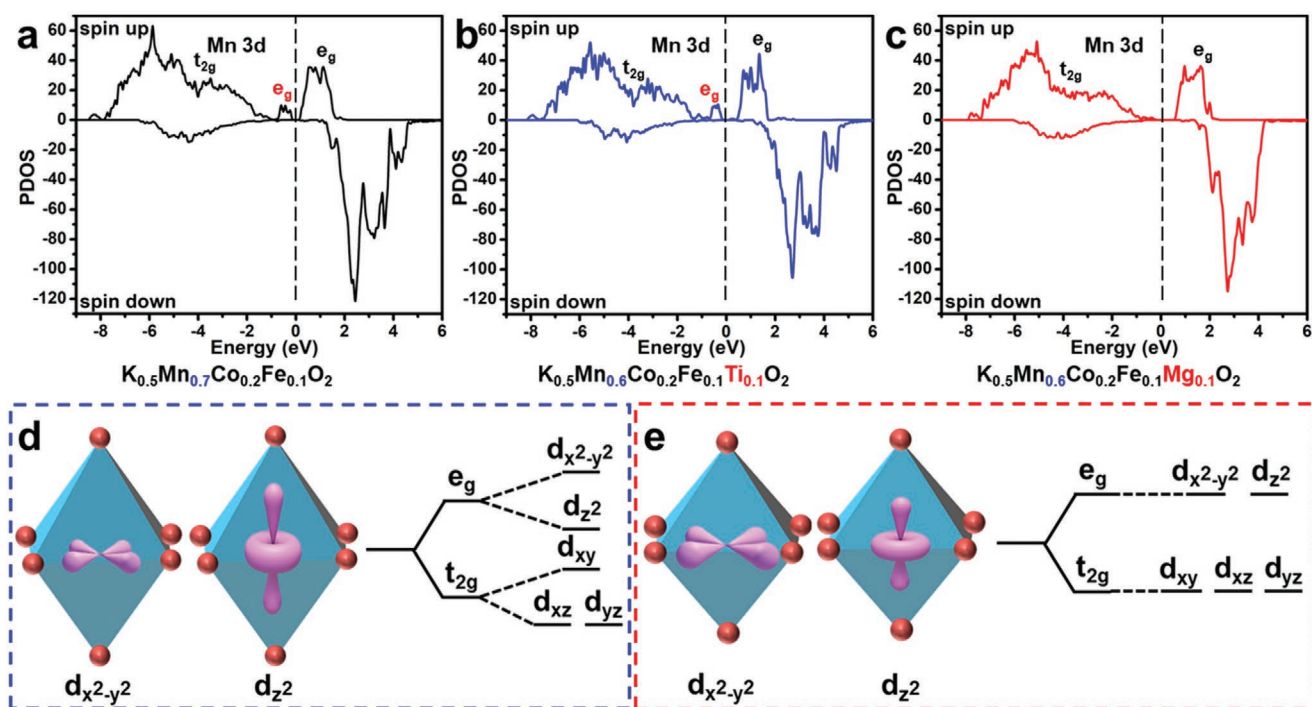


**Figure 5.** Partial density of states of Mn 3d electronic orbital in a)  $K_{0.5}Mn_{0.7}Co_{0.2}Fe_{0.1}O_2$ , b)  $K_{0.5}Mn_{0.6}Co_{0.2}Fe_{0.1}Ti_{0.1}O_2$ , and c)  $K_{0.5}Mn_{0.6}Co_{0.2}Fe_{0.1}Mg_{0.1}O_2$ , respectively. Fermi level located at zero energy. Schematic of d)  $Mn^{3+}$  and e)  $Mn^{4+}$  electronic configurations and visualization of Jahn–Teller distortion.

Mn with  $Ti^{4+}$  and  $Mg^{2+}$  ions (common structural stabilizers) in  $K_{0.5}Mn_{0.7}Co_{0.2}Fe_{0.1}O_2$ . While the introduction of  $Ti^{4+}$  ions reduced the valence of Mn, the  $Mg^{2+}$  ions increase the Mn valence. As a result, the PIB using the  $K_{0.5}Mn_{0.6}Co_{0.2}Fe_{0.1}Mg_{0.1}O_2$  with the highest Mn valence (4+) as cathode, exhibited outstanding cycling stability with capacity retention of 91% at  $0.1\text{ A g}^{-1}$  after 150 cycles, and retained 74% of the initial capacity even after 500 cycles at  $1\text{ A g}^{-1}$ . The  $K_{0.5}Mn_{0.6}Co_{0.2}Fe_{0.1}Mg_{0.1}O_2$  with the highest Mn valence experiences a highly reversible single-phase reaction upon  $K^+$  deintercalation/intercalation. The first-principles calculations demonstrate that the enhanced phase stability and cycling performance are ascribed to the suppressed Jahn–Teller effect by regulating Mn valence. We believe this strategy provides a new guideline for the development of advanced cathode materials for PIBs.

## Supporting Information

Supporting Information is available from the Wiley Online Library or from the author.

## Acknowledgements

Z.X., F.X., and L.X. contributed equally to this work. This work was supported by the National Natural Science Foundation of China (21905218, 51832004, and 52072282), the National Key Research and Development Program of China (2020YFA0715000), the Natural Science Foundation of Hubei Province (2020CFB519), the Hainan Provincial Joint Project of Sanya Yazhou Bay Science and Technology City (520LH055), the Sanya Science and Education Innovation Park of Wuhan University of Technology (2020KF0019), the Foshan Xianhu

Laboratory of the Advanced Energy Science and Technology Guangdong Laboratory (XHT2020-003), the Fundamental Research Funds for the Central Universities (WUT: 2020IVB034, 2020IVA036, 2021CG014, and 2021-LX-B1-08), State Key Laboratory of Advanced Technology for Materials Synthesis and Processing (WUT: 2020-KF-4). The S/TEM work was performed at the Nanostructure Research Center (NRC), which is supported by the Fundamental Research Funds for the Central Universities (WUT: 2021III1016GX).

## Conflict of Interest

The authors declare no conflict of interest.

## Data Availability Statement

Research data are not shared.

## Keywords

Jahn–Teller effect, long-term cycling stability, Mn-based layered cathodes, potassium-ion batteries, valence regulating

Received: August 18, 2021

Revised: November 10, 2021

Published online:

- [1] T. Hosaka, K. Kubota, A. S. Hameed, S. Komaba, *Chem. Rev.* **2020**, 120, 6358.
- [2] S. Dhir, S. Wheeler, I. Capone, M. Pasta, *Chem* **2020**, 6, 2442.

- [3] L. Mai, M. Yan, Y. Zhao, *Nature* **2017**, 546, 469.
- [4] R. Rajagopalan, Y. Tang, X. Ji, C. Jia, H. Wang, *Adv. Funct. Mater.* **2020**, 30, 1909486.
- [5] J. Xu, S. Dou, X. Cui, W. Liu, Z. Zhang, Y. Deng, W. Hu, Y. Chen, *Energy Storage Mater.* **2021**, 34, 85.
- [6] W. Li, Z. Bi, W. Zhang, J. Wang, R. Rajagopalan, Q. Wang, D. Zhang, Z. Li, H. Wang, B. Wang, *J. Mater. Chem. A* **2021**, 9, 8221.
- [7] J. Liao, Y. Han, Z. Zhang, J. Xu, J. Li, X. Zhou, *Energy Environ. Mater.* **2021**, 4, 178.
- [8] H. Kim, J. C. Kim, M. Bianchini, D.-H. Seo, J. Rodriguez-Garcia, G. Ceder, *Adv. Energy Mater.* **2018**, 8, 1702384.
- [9] Z. Liu, H. Su, Y. Yang, T. Wu, S. Sun, H. Yu, *Energy Storage Mater.* **2021**, 34, 211.
- [10] X. Zhang, Z. Wei, K. N. Dinh, N. Chen, G. Chen, F. Du, Q. Yan, *Small* **2020**, 16, 2002700.
- [11] B. Wang, Y. Peng, F. Yuan, Q. Liu, L. Sun, P. Zhang, Q. Wang, Z. Li, Y. A. Wu, *J. Power Sources* **2021**, 484, 229244.
- [12] Z. Xiao, J. Meng, F. Xia, J. Wu, F. Liu, X. Zhang, L. Xu, X. Lin, L. Mai, *Energy Environ. Sci.* **2020**, 13, 3129.
- [13] L. Deng, T. Wang, Y. Hong, M. Feng, R. Wang, J. Zhang, Q. Zhang, J. Wang, L. Zeng, Y. Zhu, L. Guo, *ACS Energy Lett.* **2020**, 5, 1916.
- [14] H. Kim, D. H. Seo, J. C. Kim, S. H. Bo, L. Liu, T. Shi, G. Ceder, *Adv. Mater.* **2017**, 29, 1702480.
- [15] S. Zhao, K. Yan, P. Munroe, B. Sun, G. Wang, *Adv. Energy Mater.* **2019**, 9, 1803757.
- [16] B. Peng, Y. Li, J. Gao, F. Zhang, J. Li, G. Zhang, *J. Power Sources* **2019**, 437, 226913.
- [17] S. Chong, Y. Wu, C. Liu, Y. Chen, S. Guo, Y. Liu, G. Cao, *Nano Energy* **2018**, 54, 106.
- [18] K. Lei, Z. Zhu, Z. Yin, P. Yan, F. Li, J. Chen, *Chem* **2019**, 5, 3220.
- [19] C. Liu, S. Luo, H. Huang, Y. Zhai, Z. Wang, *Chem. Eng. J.* **2019**, 356, 53.
- [20] X. Wang, X. Xu, C. Niu, J. Meng, M. Huang, X. Liu, Z. Liu, L. Mai, *Nano Lett.* **2017**, 17, 544.
- [21] T. Deng, X. Fan, J. Chen, L. Chen, C. Luo, X. Zhou, J. Yang, S. Zheng, C. Wang, *Adv. Funct. Mater.* **2018**, 28, 1800219.
- [22] C. Liu, S. Luo, H. Huang, X. Liu, Y. Zhai, Z. Wang, *Chem. Eng. J.* **2019**, 378, 122167.
- [23] J.-Y. Hwang, J. Kim, T.-Y. Yu, H.-G. Jung, J. Kim, K.-H. Kim, Y.-K. Sun, *J. Mater. Chem. A* **2019**, 7, 21362.
- [24] J. U. Choi, J. Kim, J.-Y. Hwang, J. H. Jo, Y.-K. Sun, S.-T. Myung, *Nano Energy* **2019**, 61, 284.
- [25] X. Zhang, Y. Yang, X. Qu, Z. Wei, G. Sun, K. Zheng, H. Yu, F. Du, *Adv. Funct. Mater.* **2019**, 29, 1905679.
- [26] M. G. T. Nathan, N. Naveen, W. B. Park, K.-S. Sohn, M. Pyo, *J. Power Sources* **2019**, 438, 226992.
- [27] Q. Deng, F. Zheng, W. Zhong, Q. Pan, Y. Liu, Y. Li, G. Chen, Y. Li, C. Yang, M. Liu, *Chem. Eng. J.* **2020**, 392, 123735.
- [28] H. V. Ramasamy, B. Senthilkumar, P. Barpanda, Y.-S. Lee, *Chem. Eng. J.* **2019**, 368, 235.
- [29] Y.-S. Xu, Y.-N. Zhou, Q.-H. Zhang, M.-Y. Qi, S.-J. Guo, J.-M. Luo, Y.-G. Sun, L. Gu, A.-M. Cao, L.-J. Wan, *Chem. Eng. J.* **2021**, 412, 128735.
- [30] P.-F. Wang, Y. You, Y.-X. Yin, Y.-G. Guo, *Adv. Energy Mater.* **2018**, 8, 1701912.
- [31] P.-F. Wang, T. Jin, J. Zhang, Q.-C. Wang, X. Ji, C. Cui, N. Piao, S. Liu, J. Xu, X.-Q. Yang, *Nano Energy* **2020**, 77, 105167.
- [32] Y. Liu, C. Wang, S. Zhao, L. Zhang, K. Zhang, F. Li, J. Chen, *Chem. Sci.* **2021**, 12, 1062.
- [33] K. Zhang, D. Kim, Z. Hu, M. Park, G. Noh, Y. Yang, J. Zhang, V. W.-h. Lau, S.-L. Chou, M. Cho, S.-Y. Choi, Y.-M. Kang, *Nat. Commun.* **2019**, 10, 5203.
- [34] L. Wang, Y.-G. Sun, L.-L. Hu, J.-Y. Piao, J. Guo, A. Manthiram, J. Ma, A.-M. Cao, *J. Mater. Chem. A* **2017**, 5, 8752.
- [35] Y. Shi, Z. Zhang, P. Jiang, A. Gao, K. Li, Q. Zhang, Y. Sun, X. Lu, D. Cao, X. Lu, *Energy Storage Mater.* **2021**, 37, 354.
- [36] P. F. Wang, H. R. Yao, X. Y. Liu, J. N. Zhang, L. Gu, X. Q. Yu, Y. X. Yin, Y. G. Guo, *Adv. Mater.* **2017**, 29, 1700210.
- [37] Q. Zhang, C. Didier, W. K. Pang, Y. Liu, Z. Wang, S. Li, V. K. Peterson, J. Mao, Z. Guo, *Adv. Energy Mater.* **2019**, 9, 1900568.
- [38] P. Bai, K. Jiang, X. Zhang, J. Xu, S. Guo, H. Zhou, *ACS Appl. Mater. Interfaces* **2020**, 12, 10490.
- [39] Y. S. Xu, J. C. Gao, X. S. Tao, Y. G. Sun, Y. Liu, A. M. Cao, L. J. Wan, *ACS Appl. Mater. Interfaces* **2020**, 12, 15313.
- [40] J. Weng, J. Duan, C. Sun, P. Liu, A. Li, P. Zhou, J. Zhou, *Chem. Eng. J.* **2020**, 392, 123649.
- [41] Y.-S. Xu, Q.-H. Zhang, D. Wang, J.-C. Gao, X.-S. Tao, Y. Liu, Y.-G. Sun, L. Gu, B.-B. Chang, C.-T. Liu, S.-Q. Shi, A.-M. Cao, *Energy Storage Mater.* **2020**, 31, 20.
- [42] R. Dang, N. Li, Y. Yang, K. Wu, Q. Li, Y. L. Lee, X. Liu, Z. Hu, X. Xiao, *J. Power Sources* **2020**, 464, 228190.
- [43] S. Xu, C. Bao, M. Yu, S. Liu, L. Chen, D. Zhang, *Mater. Lett.* **2020**, 270, 127733.
- [44] Z. Xiao, J. Meng, Q. Li, X. Wang, M. Huang, Z. Liu, C. Han, L. Mai, *Sci. Bull.* **2018**, 63, 46.
- [45] J. U. Choi, J. Kim, J. H. Jo, H. J. Kim, Y. H. Jung, D.-C. Ahn, Y.-K. Sun, S.-T. Myung, *Energy Storage Mater.* **2020**, 25, 714.
- [46] W.-W. Liu, D. Wang, Z. Wang, J. Deng, W.-M. Lau, Y. Zhang, *Phys. Chem. Chem. Phys.* **2017**, 19, 6481.